Robust Interfacial Effect in Multi-Interface Environment through Hybrid Reconstruction Chemistry for Enhanced Energy Storage

Wei Guo[a]*, Chaochao Dun[b], Feipeng Yang[c], Cheng Zhan[d,e]*, Jeffrey J. Urban[b], Jinghua Guo[c], Qiuyu Zhang[a]*

[a]Key Laboratory of Special Functional and Smart Polymer Materials of Ministry of Industry and Information Technology, School of Chemistry and Chemical Engineering, Northwestern Polytechnical University, Xi'an 710072 China.

[b]The Molecular Foundry, Lawrence Berkeley National Laboratory, Berkeley, CA 94720, USA.

[c]Advanced Light Source, Lawrence Berkeley National Laboratory, Berkeley, CA 94720, USA.

[d]School of Science, Nanjing University of Science and Technology, Nanjing 210094, China.

[e]MIIT Key Laboratory of Semiconductor Microstructure and Quantum Sensing, Department of Applied Physics, Nanjing University of Science and Technology, Nanjing 210094, China.

Correspondence and requests for materials should be addressed to W. Guo (weiguo-nwpu@nwpu.edu.cn), C. Zhan (czhan@njust.edu.cn), and Q. Zhang (qyzhang@nwpu.edu.cn)

ABSTRACT: Electrochemical oxidation-driven reconstruction has emerged as an efficient approach for developing advanced materials, but the reconstructed microstructure still faces challenges including inferior conductivity, unsatisfying intrinsic activity and active-species dissolution. Herein, we present hybrid reconstruction chemistry that synergistically couples electrochemical oxidation with electrochemical polymerization (EOEP) to overcome these constraints. During the EOEP process, the metal hydroxides undergo rapid reconstruction and dynamically couple of polypyrrole (PPy), resulting in an interface-enriched microenvironment. We observe that the interaction between PPy and the reconstructed metal center (i.e., Mn>Ni, Co) is strongly correlated. Theoretical calculation results demonstrate that the strong interaction between Mn sites and PPy breaks the intrinsic limitation of MnO_2, rendering MnO_2 with a metallic property for fast charge transfer and enhancing the ion-adsorption dynamics. *Operando* Raman measurement confirms the promise of the EOEP-treated $Mn(OH)_2$ (E-MO/PPy) to stably work under a 1.2 V potential window. The tailored E-MO/PPy exhibits a high capacitance of 296 F g^{-1} at a large current density of 100 A g^{-1}. Our strategy presents breakthroughs in upgrading the electrochemical reconstruction technique, which enables both activity and kinetics engineering of electrode materials for better performance in energy-related fields.

KEYWORDS: hybrid reconstruction, interface, supercapacitors, electronic transfer, MnO_2

INTRODUCTION

The booming of smart and renewable energy systems has stimulated the research efforts on the development of supercapacitors owing to the advantages of high-power density, long life span and eco-friendliness.[1-4] The performance of supercapacitors is primarily determined by the electrode materials, which typically rely on either the charge-storage mechanism of the electrostatic adsorption/desorption of the electrolyte ions (electric-double-layer-capacitors, EDLCs) or the fast surface/near-surface redox reaction (pseudocapacitors, PCs).[5-8] While PCs

offer stronger capability/activity to store and release charges, their faradic-type mechanism often results in slower electronic-transfer and ionic-transport rates compared to EDLCs. In particular, transition metal (hydr)oxides (TM-OH) are considered as the effective electrode materials of PCs due to their low cost, high redox activity and low biotoxicity. However, their practical performance is always far below their theoretical values. The root cause lies on the poorly configured structure that fails to concurrently unlock the decent intrinsic reactivity and reaction kinetics, to the best of our knowledge.

To address this issue, electrochemical oxidation presents a straightforward route for *in-situ* topology reconstruction of precursors into defective and active structures, resulting in more available active sites and enriched ion-migration channels.[9-12] However, despite its achievements, concerns regarding the microstructure evolution persist, as the *in-situ* triggered oxidative and locally strong-acidic/alkaline environment may result in the unfavorable phase transition and partial dissolution of active species (Figure 1a).[13-16] And the reconstructed microstructures are generally characterized by inferior conductivity and poor durability, leading to a performance that still falls far short of the theoretical value. An upgraded electrochemical oxidation reaction system is required to ensure the optimal activity and reaction kinetics for the reconstructed phase structure, which is crucial for the development and broad applications of energy materials.

Recent studies have shown that the conductive polymer network can be controllably tailored onto inorganic material matrix,[17-20] and their intimate interaction by *in-situ* nucleation/assembly or superlattice engineering can create a synergy mechanism that enhances energy-storage performance.[21-24] However, the traditional strategy for organic/inorganic coupling only tailors in the micro/nano-scale, leaving the large portion of active sites in the bulk region inactivated and blocked from contact with the conductive polymer network. This finally results in the highly limited interfacial effects.[25] Fortunately, electrochemically reconstructed microstructure is always loose, defective and rich in active surface with coordinatively unsaturated sites.

Therefore, it is predicted that the molecular-level coupling can be realized and the available interfacial effects between the reconstructed phase and the conductive polymer will be maximized, thus leading to a huge promotion of the charge-storage capabilities including reaction dynamics, reactivity and stability. Besides, the robust interaction with the conductive polymer network will contribute to facilitating charge transfer and restraining the self-aggregation during the reconstruction, which deepens the surface-to-bulk transformation to expose more electrochemically active sites. The above information indicates that there is great promise in synergistically coupling electrochemical polymerization engineering with the electrochemical oxidation process *in situ* to boost the development of advanced materials (Figure 1a). Beyond the hybrid reconstruction concept, it is highly desirable to provide comprehensive atomic/molecular-level elucidation of the dynamic microstructure evolution and interfacial interaction by adopting cutting-edge techniques, which will guide the fast and sustainable development of energy-related fields.

In this work, we introduce an electrochemical oxidation-coupled electrochemical polymerization (EOEP) to optimize the reconstruction of transition metal hydroxides. Using $Mn(OH)_2$ as a proof-of-concept, we identify that the EOEP process triggers fast and deep reconstruction to create a low-crystalline and active-site-rich microstructure interconnected with polypyrrole (PPy), resulting in the intimate organic/inorganic coupling with highly enriched hybrid interfaces. By virtue of the EOEP process, we achieve the structural reconstruction and interfacial editing of a series of transition metal hydroxides, yielding a family of emerging organic/inorganic hybrid materials. We demonstrate the reconstructed Mn sites deliver the enhanced electronic transfer with PPy when compared to that of Ni and Co sites. First-principle calculations indicate that the strong interfacial interaction overcomes the inherent limit of MnO_2 to feature the half-metallic-like electronic transfer rate as well as promoted electrolyte-ion adsorption dynamics. The *operando* electrochemical Raman measurement manifests that the well-tailored E-MO/PPy can stably work at a wide potential

window up to 1.2 V with sound reversibility. With the integrated advantages, E-MO/PPy exhibits a capacitance of 296 F g^{-1} at a large current density of 100 A g^{-1}. This hybrid reconstruction concept provides insights into the high-efficient interfacial microenvironment design for boosting ion/charge transfer toward better energy storage and conversion applications.

RESULTS AND DISCUSSION

The electro-oxidation methods have been widely adopted to reconstruct transition-metal (TM) hydroxides (TM-OH) into the corresponding (oxy)hydroxides with relatively high reactivity (E-TMO). However, relying solely on electro-oxidation may lead to the gradual leaching of active species and subsequent structure destruction, which is unfavorable for further applications. In contrast, our proposed EOEP strategy combines electro-polymerization with electro-oxidation (Figure 1a). Such an integrated process is highly efficient and value-added, which results in the *in-situ* formation of a conductive polymer layer (i.e., PPy) that provides abundant charge-transfer highways for deep reconstruction. The as-tailored structure offers several key advantages. Firstly, it generates abundant organic-inorganic hybrid interfaces within the low-crystalline structures, which enhances the intrinsic reactivity of E-TMO through robust and tunable interface effects. Secondly, the conductive polymer, with potential confinement effects, mitigates the dissolution of active species, thereby enhancing structural stability for long-term and high-rate applications. Lastly, the conductive polymer facilitates the electronic transfer of active species and contributes to an overall increase in capacitance.
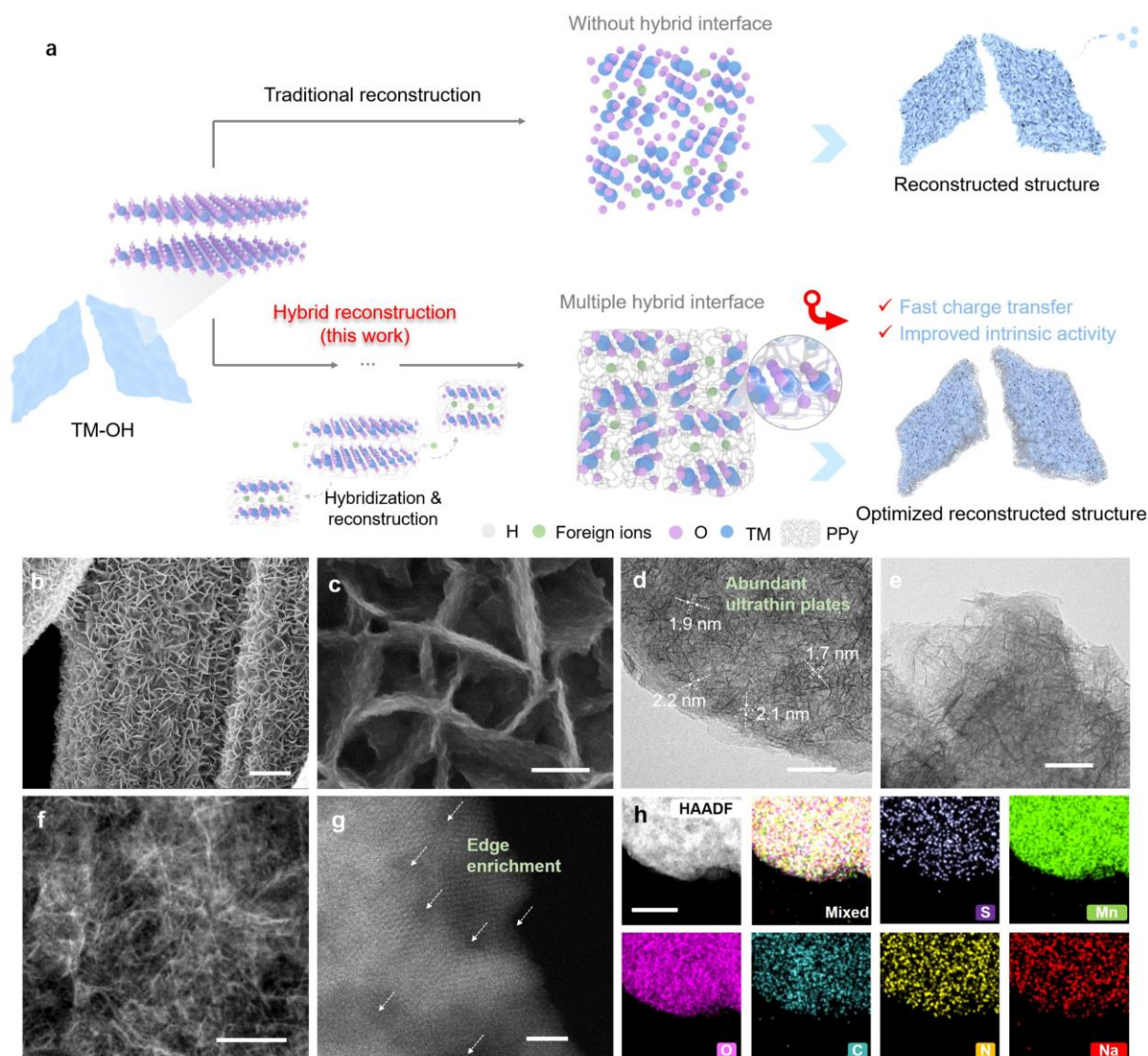
Figure 1. (a) Schematic illustrations of the conventional electrochemical oxidation and the as-proposed EOEP methods. (b-c) SEM, (d-e) TEM, (f-g) HAADF-STEM, and (h) elemental maps of the as-formed E-MO/PPy. Scale bars of (b-h) are 2 μm, 200 nm, 50 nm, 50 nm, 50 nm, 2 nm and 200 nm, respectively.

The EOEP process and mechanism were investigated by using electrodeposited manganese hydroxides (Mn-OH) as the model materials. The morphology of Mn-OH was revealed by high-angle annular dark-field scanning transmission electron microscopy (HAADF-STEM) images and elemental maps, which display the cross-linked nanosheet features of Mn-OH with a uniform distribution of Mn and O elements (Figure S1). X-ray diffraction (XRD) pattern

evidences the formation of $Mn(OH)_2$, as indicated by matching the typical peaks at 19.2, 32.5, 36.3, 38.2, 51.0 and 60.1° (JCPDS card no. 18-0787, Figure S2). Mn-OH experiences conformal transformation during the EOEP process, yielding homogenous and well-defined nanosheet arrays after 5 min of EOEP treatment (Figure 1b-c and S3a).

Transmission electron microscope (TEM) and HAADF-STEM images show the emergence of the high-stacking-density, ultra-small and thin plates on the surface of the reconstructed microstructure (Figure 1d-g and S3b), implying a topographic transformation. Notably, in contrast to the pristine Mn-OH sheets (thickness: ~30 nm; size: ~1.0 μm), these ultrathin small plates (thickness: ~2 nm; size: less than 50 nm) are available to expose enriched active sites, enabling promoted ion-diffusion/transport and electronic transfer dynamics. There also exist abundant pores in the reconstructed structure (Figure S3c-e), which further enables a faster and more efficient transport of electrolyte ions. The observable lattice fringe spacings are 0.25, 0.14 and 0.70 nm (Figure S4a-b), which align well to the (200), (310) and (001) planes of birnessite-type MnO_2. This is also evidenced by the appearance of diffraction rings of (310) and (200) in the SAED pattern (Figure S4c). The energy-dispersive X-ray (EDX) spectrum and elemental maps demonstrate the uniform distribution of Mn, O, C, N, Na and S elements (Figures S4d and 1h), implying the fine assembly/hybridization of the in-situ formed MnO_x and PPy. It is noted here that S comes from the partial diffusion and doping of counterions (SO_4^{2-}) into the PPy chains.

Moreover, the characteristic XRD peaks of $Mn(OH)_2$ become undetectable after the EOEP treatment (Figure S2), indicative of an inverse correlation between the disappearance of the $Mn(OH)_2$ and the formation of low-crystalline MnO_x. In contrast, although electrochemical oxidation alone also triggers the transformation of $Mn(OH)_2$ into a low-crystalline structure after 5 min of treatment (Figure S5), this process results in severe leaching of Mn species from the reconstructed host and restacking of the structure, which becomes more pronounced with

prolonged treatment time (Figure S6-S9). These results finely confirm the merits of the proposed EOEP process.

The evolution of fine structure during the EOEP process was validated using the soft X-ray absorption spectroscopy (sXAS) technique (Figure 2a). The surface-sensitive detection mode, i.e., total electron yield (TEY) with a detection depth of 2-5 nm is adopted. For the O K-edge spectra (Figure 2b), the pre-edge region and the broad-band region can be attributed to the hybridization between Mn_{3d} and O_{2p}, as well as Mn_{4sp} and O_{2p}, respectively. The broad band shows a positive shift after 30 s of EOEP treatment, manifesting the increased valence state of Mn sites. Subsequently, the signal at about 539.5 eV is detected and becomes gradually intensified, which is related to S=O of the doped SO_4^{2-} in the PPy matrix.[26] This is in good agreement with the TEM elemental mapping results. It is also accompanied by the emergence of the C=O (located at 531.4 eV) and C-O (located at 534.2 eV) signals,[27] which may be attributed to the partial oxidation of the carbon substrate. Moreover, according to the Mn L-edge spectra (L_3 region) in Figure 2c, the pristine Mn-OH demonstrates the co-existence of Mn^{2+} and Mn^{3+}. The Mn^{3+} peak became more intensified during the first 5 s of EOEP treatment, corresponding to the partial oxidation of Mn^{2+} to Mn^{3+}.[28, 29] The Mn^{4+} signal emerges after 30 s of treatment, then becomes more distinguishable with time, and finally remains unchanged, indicating the gradual oxidation to form stable high-valent Mn sites.

To further disclose the transformation mechanisms during the EOEP treatment, *ex-situ* XPS characterization was performed. The peak energy separation of Mn 3s displays a decrease from 5.9 to 5.1 eV (Figure S10a), manifesting the gradual oxidation of Mn sites. It is noteworthy that this final value (5.1 eV) is higher than that of electrochemical oxidation-treated Mn-OH (4.9 eV, Figure S11a), implying that there exists the potential interaction between MnO_x and PPy to modulate the surface electronic structure. This is further demonstrated by the decrease of the protonation degree as the prolonging of the reaction time (Figure S12). We then made a comparison for Mn L-edge XAS spectra of 5 min-EOEP-treated Mn-OH and 5 min-

electrochemical-oxidation-treated Mn-OH. As shown in Figure S13, the electrochemical-oxidation-treated Mn-OH is similar to the standard MnO_2 reference sample, while the EOEP-treated Mn-OH demonstrates a slight increase in peak intensity at the low energy region, further confirming the tuned surface electronic structure. Additionally, a significant negative shift of about 0.8 eV for the Mn 2p spectra of EOEP-treated Mn-OH is observed in comparison to that of electrochemical-oxidation-treated one (Figure 2e), substantiating the formation of a robust electronic interaction between MnO_x and PPy coating layer. It is also observed that the Na 1s signal became increasingly intensified for Mn-OH after the electrochemical oxidation or EOEP treatment (Figure S10b and S11d), manifesting the accommodation of Na^+ in the reconstructed MnO_x phase.[30]

The deep phase transformation of Mn-OH is verified by the negligible difference for the Raman spectra of the 2 min- and 5 min-EOEP-treated Mn-OH (Figure S14). Specifically, both show the three peaks at about 500, 575 and 646 cm^{-1}, matching well with the characteristic peaks of birnessite-type MnO_2.[31, 32] These results substantiate the successful formation of the low-crystalline MnO_2 which is intimately coupled by PPy. The evolution of the O 1s spectra is also studied to gain more insights into the dynamic reconstruction process. The high-resolution O 1s spectrum can be fitted with three doubles: lattice O (530.1 eV), lattice OH (531.6 eV) and the surface-absorbed O (533.0 eV).[33, 34] After applying the EOEP process to Mn-OH, the binding energy of lattice O demonstrates a significantly negative shift of about 0.8 eV after 1 min treatment (Figure S15). This further illustrates the robust electronic interaction during the dynamic reconstruction and self-assembly/hybridization, in good accordance with the Mn *L*-edge, Mn 3 s and Mn 2p measurement results. Another detail is the significant decrease in the peak intensity of lattice O (i.e., Mn-O bond) over time (Figure 2d), demonstrating the gradual coating of PPy onto the reconstructed MnO_2 surface during the EOEP process. The lattice O content becomes less than 5% after 5 min of EOEP treatment, implying sufficient coupling between PPy and MnO_2. The resulting 5 min-EOEP-treated Mn-OH is denoted as E-MO/PPy

for further investigations, while the 5 min-treated Mn-OH through the conventional electrochemical oxidation is referred to as E-MO for comparison.
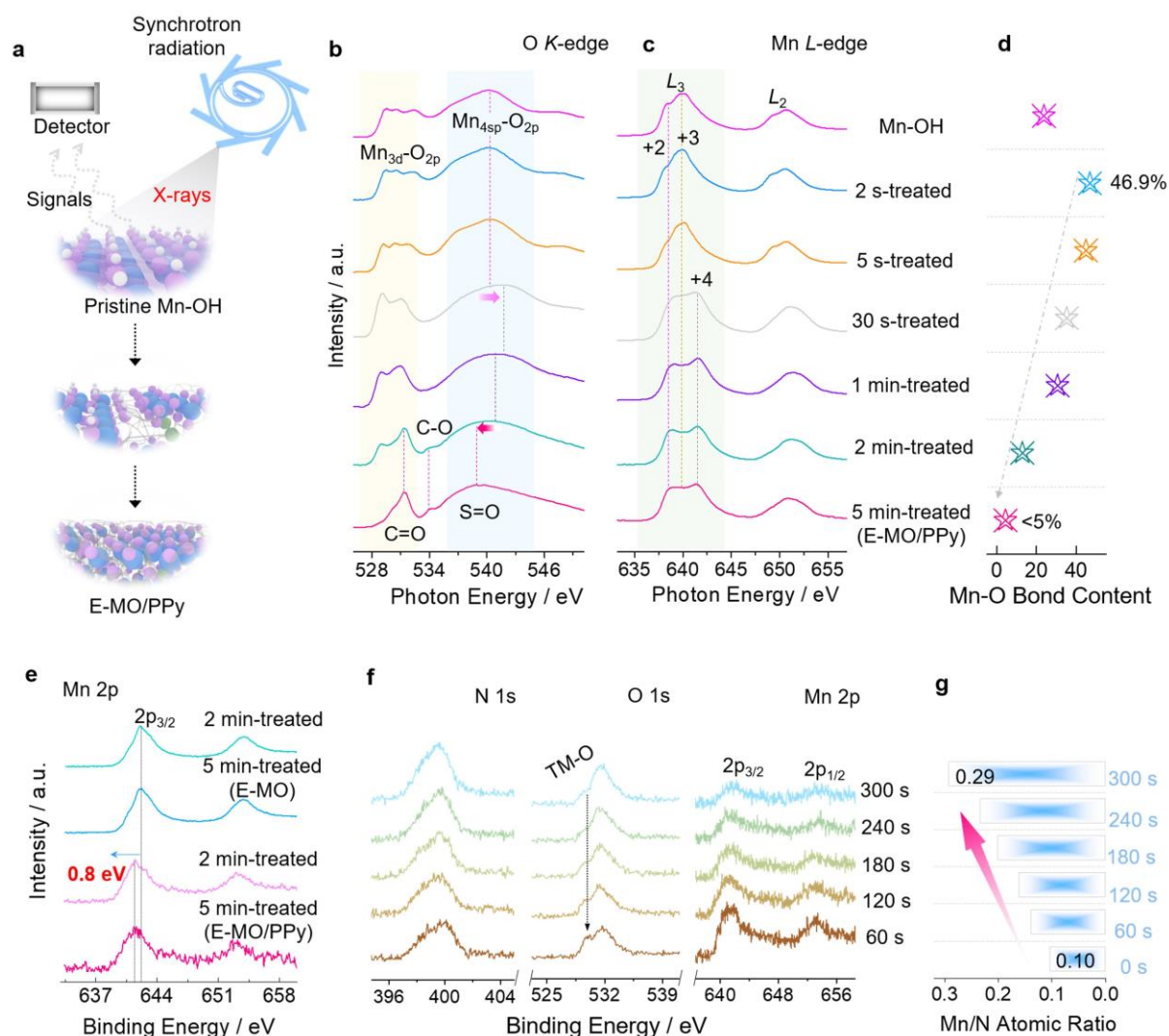

Figure 2. (a) Schematic illustration of revealing the dynamic evolution of the pristine Mn-OH during the EOEP treatment by the sXAS technique. (b) O K-edge, (c) Mn L-edge and (d) Mn-O bond contents of Mn-OH after different times of the EOEP treatment. (e) Mn 2p spectra of the 2 and 5 min-treated samples by electrochemical oxidation and EOEP process. (f) XPS depth profiles of E-MO/PPy and (g) the corresponding atomic ratios after different times of Ar$^+$ sputtering.

To gain a better understanding of the microstructure of E-MO/PPy, XPS depth profiles were collected after various durations of Ar^+ sputtering. The Mn 2p signal shows an increase in intensity with the prolonging of sputtering time (Figure 2f), indicating efficient coupling of PPy over the reconstructed MnO_2. A similar trend was observed for O 1s spectra, where the characteristic peak related to lattice O of the derived MnO_2 (as discussed in Figure S15) became more pronounced as the etching depth increases. This is supported by the gradual increase in the Mn/N atomic ratio (Figure 2g). Besides, the high intensity of N 1s spectra remains at different etching depths (Figure 2f), confirming the efficient and uniform coupling of the derived MnO_2 with PPy.

The results presented above highlight the potential of our EOEP strategy for the configuration of advanced organic/inorganic hybridized structures. To further expand the application, we synthesized a series of transition-metal hydroxides (Ni-OH, Co-OH, NiCo-OH and CoMn-OH) by following our previous method,[12, 35] and investigated their structures with EOEP treatment (yielding E-NO/PPy, E-CO/PPy, E-NCO/PPy and E-MCO/PPy, respectively) as illustrated in Figure 3a. For comparison, samples formed by the traditional electrochemical oxidation process were named E-NO, E-CO, E-NCO and E-MCO, respectively. The resulting structure transformations were carefully studied (Figure 3b), and the detailed discussion is included in Figures S16-S20. Furthermore, the depth XPS profiles were analyzed. For each case, the effective hybridization of PPy and the derived active (oxy)hydroxides was revealed by the distinguishable N 1s peaks that remained with the increasing etching depth. This was further confirmed by the improved lattice O feature and the rising atomic ratio of transition-metal to N as the etching depth increases (Figure 3c-d).
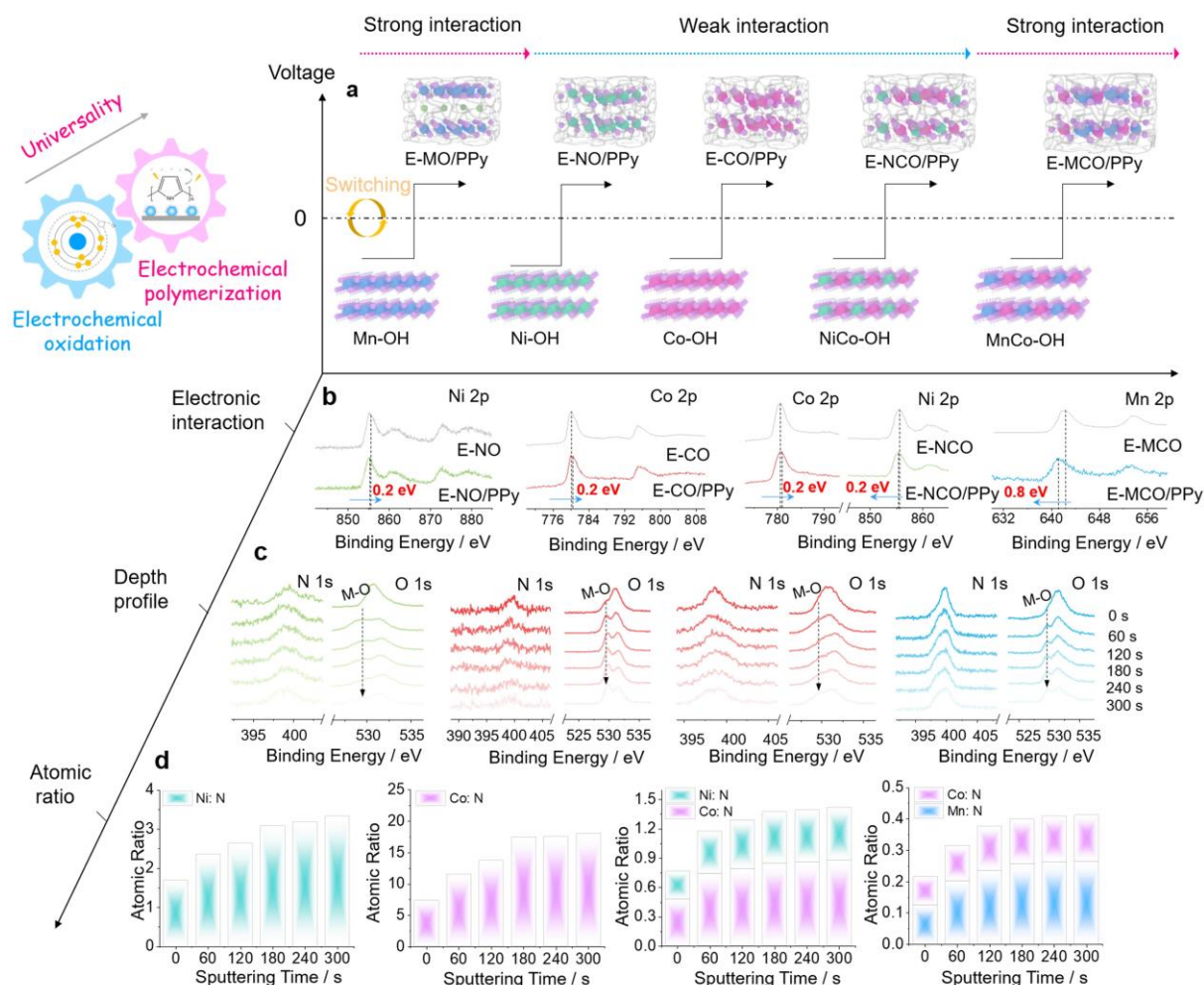
Figure 3. (a) Schematic illustration for the applications of EOEP method. Multi-scale characterizations of the as-formed (from left to right) E-NO/PPy, E-CO/PPy, E-NCO/PPy and E-MCO/PPy: (b) comparisons of transition-metal 2p XPS spectra for samples made by traditional electrochemical oxidation and EOEP process, (c) XPS depth profiles and (d) the corresponding atomic ratios after different sputtering times.

It is worth noting that there is a significant variation in the potential interaction between the metal sites and PPy. The Ni 2p spectrum of E-NO/PPy demonstrates a slight negative shift of only 0.2 eV when compared with that of E-NO/PPy (Figure 3b), indicative of a weak interaction between Ni sites and PPy. Similarly, a slight positive shift of 0.2 eV of Co 2p spectrum was found for E-CO/PPy when compared with that of E-Co. The weak interaction of Ni/Co sites and PPy is further verified by the same subtle shift (0.2 eV) of Ni 2p and Co 2p spectra of E-

NCO/PPy in comparison to those of E-NCO. In sharp contrast, the Mn 2p spectrum of E-MCO/PPy exhibits a significantly negative shift of 0.8 eV in comparison to that of E-MCO, which is in good agreement with the comparison result of E-MO/PPy and E-MO (Figure 2e). Moreover, highly decreased atomic ratios of Mn/N are found in comparison to the cases of Co/N and Ni/N at different etching depths (Figure 3d), indicative of a more efficient and uniform coating of PPy onto Mn sites. The results finely confirm the highly enhanced interaction of Mn sites toward PPy compared to that of Ni and Co sites, which ultimately enables a more intimate and uniform organic/inorganic coupling and assembly.

The electrochemical performances were evaluated in a three-electrode configuration in 1 M Na_2SO_4 electrolyte. The cyclic voltammetry (CV) measurements show the sound charge/discharge reversibility and rate capability of E-MO/PPy, which can stably and finely work at a super-high scan rate of up to 500 mV s^{-1} within a wide potential window of 1.2 V (Figure 4a). Upon comparison of the electrochemical properties of Mn-OH treated with EOEP process for 2, 5 and 20 minutes, it was observed that the 5 min-EOEP-treated Mn-OH yielded the best capacitive contribution and ion/charge-transfer dynamics (Figure 4b, Figure S21 and S22a-b). This was attributed to the deep structure reconstruction and the moderate yet efficient PPy coupling.

Moreover, the capacitive contributions of E-MO/PPy are considerably higher than those of Mn-OH and E-MO, reaching as high as 82% at 10 mV s^{-1} and 90% at 30 mV s^{-1} (Figure 4c and S23). Furthermore, for each voltage, the response current density and the scan rate also follow the relationship as below:[36]

$$i = a v^b \qquad (1)$$

Here, a and b are constant. The b value can indicate the capacitive-controlled (b near 1) or diffusion-controlled process (b near 0.5). Figure 4d gives b values at different operation voltages for E-MO/PPy. It shows that all b values are higher than 0.75 at different voltages, and greater than 0.9 within the voltage range of 0.05 to 0.82 V, manifesting a reaction process

controlled by surface reaction. These b values are consistent with capacitive contribution results, revealing the fast-redox dynamics of E-MO/PPy for reversible and efficient energy storage.

To further understand the redox reaction behavior, the electrochemical impedance spectroscopy (EIS) measurement was performed. The Warburg factor (σ), which is inversely proportional to the ion-diffusion coefficient, can be determined by the following equation:[37]

$$Z'=R_{e}+R_{ct}+\sigma\omega^{-1/2} \tag{2}$$

Here, Z', R_{e}, R_{ct} and ω represent the real-part impedance, the equivalent resistance, the charge-transfer resistance and the angular frequency, respectively. Accordingly, by plotting Z' against $\omega^{-1/2}$, σ (the slope) can be obtained after linear fitting. As shown in Figure 4e and Figure S22c, E-MO/PPy achieves a highly decreased σ value of only 5.000, in comparison to that of E-MO (7.631), the pristine Mn-OH (13.876), 2 min-EOEP-treated Mn-OH (5.929), and 20 min-EOEP-treated Mn-OH (6.130), indicative of the highly improved ion-transport kinetics. We also quantified the charge-storage capacitances at different current densities. Encouragingly, E-MO/PPy features a high specific capacitance of 418 F g^{-1} at 1 A g^{-1}, and maintains a value of 296 F g^{-1} at an extremely high current density of 100 A g^{-1} with a retention rate of 71%, superior to those of E-MO and Mn-OH (Figure 4f and Figure S24). The great promise of E-MO/PPy is also evidenced by its sound performances in a 2 M LiNO$_3$ electrolyte (Figure S25). Additionally, E-MO/PPy shows a capacitance retention rate of 85% after 12000 cycles at 50 mV s^{-1} (a fade rate of ~0.001% per cycle, Figure S26). We believe that by further refining the hybrid reconstruction chemistry and optimizing the microstructure topology, we may potentially achieve an even better balance between activity, dynamics, and cycle stability.

For comparison, the pure PPy has been formed on the carbon fiber by electro-polymerization for 10 min. The SEM images show the carbon fiber with PPy coating well keeps its original morphology while the surface becomes rougher to some degree than before (Figure S27), indicative of the uniform distribution of the coating layer and their intimate contact. It was found that the PPy coating alone exhibited inferior charge-storage capability and the low-

crystalline MnO₂ phase played a major role in providing the high capacitance (Figure S28). When compared with relative results of manganese (hydr)oxide and MnO₂/PPy in literature, the tailored E-MO/PPy displays the capability to work under large current densities and a wide voltage window (Figure S29, Table S1-S2).
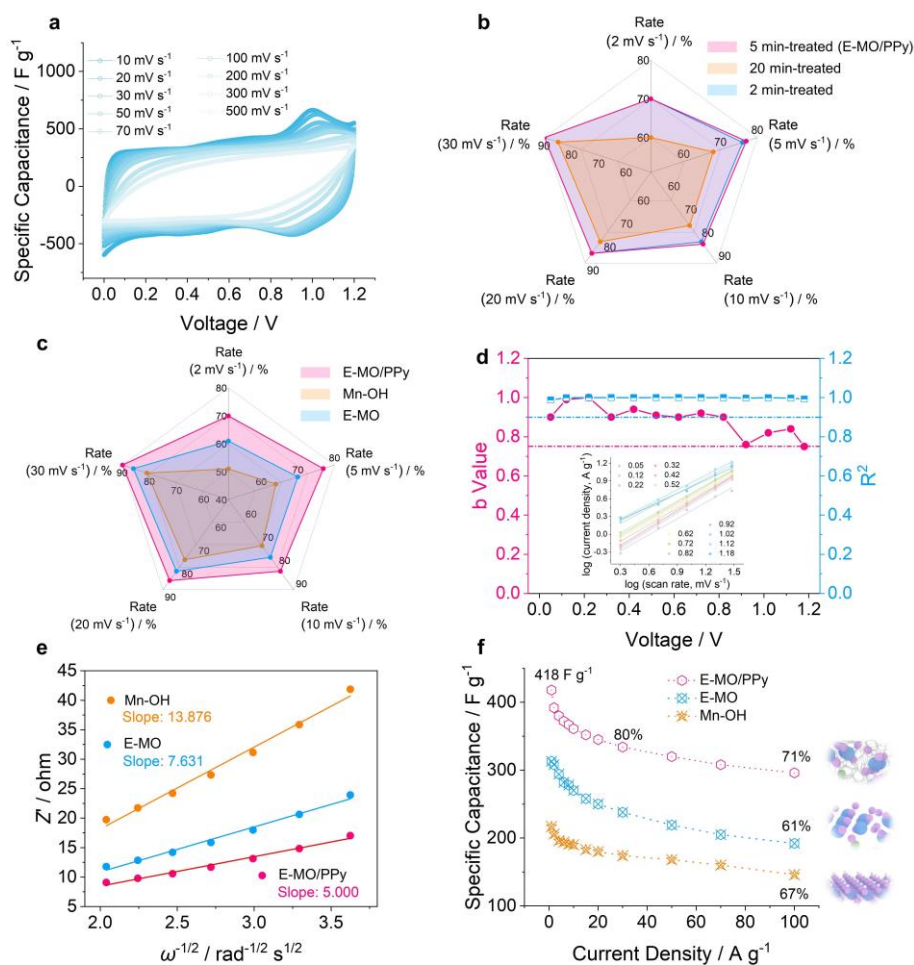

Figure 4. (a) CV curves of E-MO/PPy at different scan rates. (b) A comparison of capacitive contributions for Mn-OH treated by EOEP process for 2 min, 5 min and 20 min. (c) A comparison of capacitive contributions for Mn-OH, E-MO and E-MO/PPy at different scan rates. (d) b values calculated at different voltages (inset shows the linear relationship of logarithm current densities and logarithm scan rates). (e) Linear relationship of Z' and $\omega^{-1/2}$ for determination of Warburg factor σ. (f) Specific capacitances of E-MO/PPy, E-MO, Mn-OH at different current densities.

The electrochemical measurements have demonstrated that the developed E-MO/PPy can achieve high-efficient and stable energy storage over a wide potential window of 1.2 V. To unravel the underlying mechanism, we first conducted *operando* electrochemical Raman characterization during the charging process. As shown in Figure 5a-b, the peak at 588 cm^{-1} (v_2), assigned to the stretching vibration of MnO_6 basal plane, demonstrates a red shift to 574 cm^{-1} and becomes more intensive as the potential increases from 0 V to 1.2 V. This indicates the oxidation of Mn sites accompanied by the extracting of Na$^+$ from the interlayer.[38, 39] Besides, the dominated peak in the range of 635-665 cm^{-1} (out-of-plane Mn-O stretching, v_1) demonstrates a significant red shift with gradually decreasing intensity compared to v_2 over time, indicative of the reduced interlayer space and the weakened ordering along the interlayer interaction after the oxidation.[31, 40, 41] The fully charged E-MO/PPy was then relaxed immediately without the addition of external voltage, and the *operando* Raman spectra were collected at different relaxation times. Even after a long relaxation time of 10 min, the typical Raman peaks demonstrate negligible changes (Figure 5c and Figure S30), indicating its robust capability to work under a wide voltage window.

Furthermore, the stability of E-MO/PPy after 10 CV cycles are demonstrated by the absence of any noticeable shift in the Mn 2p spectrum, as well as the well-maintained peak energy separation of Mn 3s spectrum and the reserved N$^+$/N ratio derived from the N 1s spectrum (Figure S31a, c and d). The Na 1s spectrum also remains intensive, indicating the retained Na content after cycling (Figure S31b). Additionally, the cycled E-MO/PPy shows similar Raman signals with slightly strengthened characteristic peak intensity (Figure S32), suggesting that the basal and interlayer interaction has self-adjusted to some extent after multiple charge/discharge processes. Overall, these results suggest that E-MO/PPy exhibits decent charge/discharge stability, in good accordance with the high-rate and fast reaction dynamics.

We examined the surface potential using Kelvin probe force microscopy (KPFM) to further reveal the origin of the promoted charge storage, which is capable of detecting the surface/subsurface potentials with millivolt sensitivity. As shown in Figure 5d-g, the measured contact potential difference (CPD, between the tip and the sample) for E-MO/PPy (79 mV) is highly increased in comparison to that of E-MO, indicating the generation of the stronger potential charge transfer within the E-MO/PPy microstructure.[42, 43] To gain a more profound understanding of the organic/inorganic interfacial interaction in E-MO/PPy, we utilized First-principles calculation to study the electronic structure and interfacial charge transfer in the PPy-coupled MnO_2 heterostructure (MnO_2-PPy). The charge density difference of MnO_2-PPy was presented in Figure 5h, where the yellow and cyan regions represent the electron accumulation (grain electron) and depletion (lose electron) respectively. According to the Bader charge analysis, it is evident that there is a significant electron transfer of 0.83 e^- from PPy to MnO_2, indicating a strong interfacial coupling and binding between PPy and MnO_2 substrate, which could benefit ion transport and charge storage in supercapacitor, as reported in literatures.[44, 45]

To better comprehend the role of interfacial coupling, we compared the density of states (DOS) for the individual PPy, individual MnO_2 and MnO_2-PPy. As shown in Figure 5i, the Fermi level of an individual MnO_2 and PPy were -8.12 eV and -3.91 eV vs. vacuum level. Upon the formation of PPy-MnO_2 heterostructure, the Fermi level changed to -5.62 eV due to the electron transfer from PPy to MnO_2, leading to the transition from semiconductor (MnO_2) to metal-like (PPy-MnO_2), as illustrated by Figure S33. The transferred electrons were observed to enter into the unoccupied spin-up Mn orbits as demonstrated by the pDOS analysis in Figure S34.
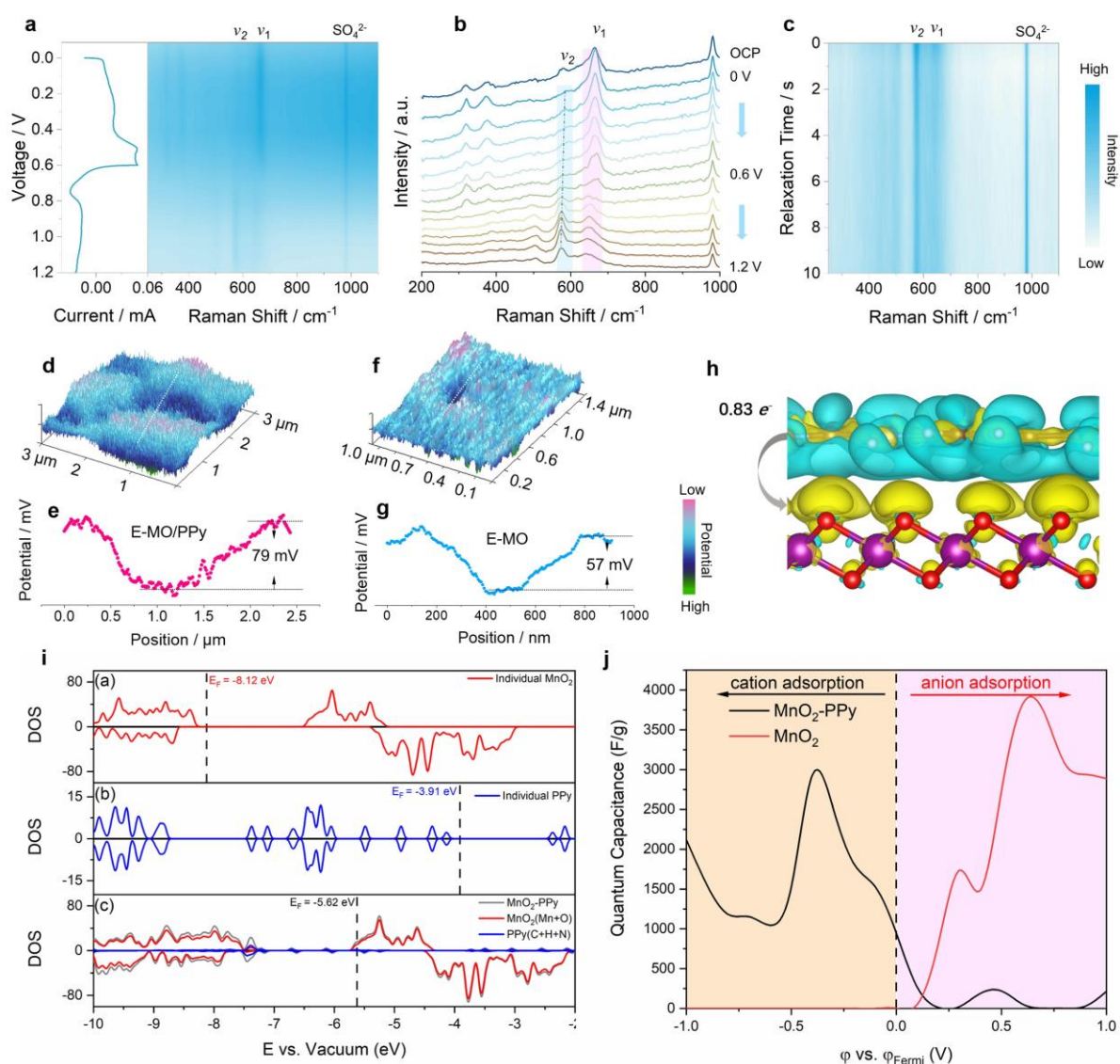
Figure 5. (a) *Operando* Raman contour project and (b) the corresponding spectra of E-MO/PPy during the charging process. (c) *Operando* Raman contour project collected for the 1.2 V-charged E-MO/PPy during the relaxation process without external voltage. 3D CPD contour projects and the corresponding line-scan CPD distribution curves of (d-e) E-MO/PPy and (f-g) E-MO. (h) Charge-density difference of MnO₂-PPy. (i) DOS curves of the individual MnO₂, individual PPy and MnO₂-PPy. (j) Quantum capacitances of the individual MnO₂ and MnO₂-PPy at different voltages (vs. φ_{Fermi}).

To explore how the change of electronic DOS affects the capacitance, we adopted the fix-band approximation to compute the quantum capacitance of MnO₂ and PPy-MnO₂ based on prior

theoretical works.[46-48] In the negative potential range, the calculated results showed that the introduction of PPy significantly enhances the quantum capacitance of MnO_2 (Figure 5j), which benefits the charge storage of cation adsorption. This is in agreement with previous studies, which reported the enhanced theoretical quantum capacitance and measured capacitance by loading the redox-active organic compounds.[49] Thus, our calculation results demonstrate good consistency with our experimental observation of improved capacitive performance and enhanced mass and charge-transport rate for the tailored E-MO/PPy microstructure.

CONCLUSIONS

In summary, a hybrid reconstruction chemistry of transition metal hydroxide precursor was developed by synergistically coupling electrochemical oxidation with electrochemical polymerization to create an optimized reaction system. This integrated process enables *in-situ* topotactic conversion of $Mn(OH)_2$ to low-crystalline MnO_2 which is fully interconnected with conductive PPy, achieving intimate and sufficient organic/inorganic coupling. The universality of our strategy was confirmed by the successful development of a series of advanced organic/inorganic heterostructures. The strong coupling observed in Mn sites allows for uniform and stable coating of PPy, accompanied by modulation of MnO_2 to greatly enhance charge-transfer and ion-adsorption/migration ability. The *operando* Raman technique aided in understanding the stable and reversible charge-storage of E-MO/PPy under a wide potential window of 1.2 V. The developed E-MO/PPy overcomes the trade-off between reactivity and durability, achieving a record-level high specific capacitance of 296 F g^{-1} at a large current density of 100 A g^{-1}. While the EOEP technique is still in its early stages, the organic/inorganic coupling concept through a "win-win" integrated reaction system can help accelerate the development of energy storage and conversion technologies.

METHODS AND EXPERIMENTAL SECTION

Chemicals and Materials. Manganous nitrate solution ($Mn(NO_3)_2$, AR, 50 wt% in H_2O) and $Co(NO_3)_2 \cdot 6H_2O$ (AR, 99%) were supplied by Aladdin Industrial Co., Ltd. $Ni(NO_3)_2 \cdot 6H_2O$ (AR, 98%) and sodium sulfate anhydrous (Na_2SO_4, AR, 99%) were supplied by Guangdong Guanghua Sci-Tech Co., Ltd. Pyrrole (AR, 99%) was supplied by Shanghai Macklin Biochemical Co., Ltd. Carbon fiber (HCP030N) was supplied by Shanghai Hesen Electric Co., Ltd. The above-mentioned chemicals or materials were used directly after purchase without further treatment or purification.

Synthesis of Mn-OH. The reaction environment was optimized by changing the reaction time, the concentration and mole ratio of the electrolytes as well as the reaction voltage. First, a piece of carbon fiber (2×3.3 cm^2) was functionalized by following the previously reported process,[50] with an aim to produce a hydrophilic surface. The pre-treated carbon fiber was then washed with deionized water and ethanol for several times, and dried at room temperature. The electrodeposition formation of Mn-OH was performed in a three-electrode configuration. The pre-treated carbon fiber, a saturated calomel electrode (SCE) and a Pt sheet electrode ($20 \times 20 \times 0.1$ mm^3) were used as the working electrode, reference electrode and counter electrode, respectively. The electrolyte was prepared by dissolving 358 mg $Mn(NO_3)_2$ solution (50 wt%) into 50 mL deionized water under the continuous stirring. The reaction was conducted under a constant voltage of -1.5 V for 10 min. After the reaction, the sample was carefully washed with water and ethanol for several times, and then dried at room temperature to obtain the light-brown Mn-OH.

Synthesis of E-MO and E-MO/PPy. E-MO/PPy was prepared by the EOEP process in a three-electrode system with the synthesized Mn-OH as the working electrode, a Pt sheet electrode ($20 \times 20 \times 0.1$ mm^3) as the counter electrode and a SCE as the reference

electrode. The electrolyte was prepared by dissolving 30 mg of pyrrole into 50 mL 1 M

Na_2SO_4 aqueous solution under continuous stirring for 1 h. The EOEP process was

performed at a constant voltage of 1.5 V for 5 min. After the reaction was completed,

the sample was washed carefully by water and ethanol for several times, and dried at

room temperature to obtain dark-brown E-MO/PPy. The formation of E-MO by

electrochemical oxidation was similar to that of E-MO/PPy, except for the absence of

PPy in the reaction electrolyte. The pure PPy was formed on the carbon fiber through a

procedure similar to the EOEP process for 10 min, excluding Mn-OH. The mass

loadings of Mn-OH, E-MO, and E-MO/PPy are in the range of 0.65-0.75 mg cm^{-2}. The

high mass loading E-MO/PPy can be configured by extending the electrodeposition time.

Material and Electrochemical Characterizations. A series of facilities or instruments

were applied for the characterization of the synthesized materials, including XRD

(Bruker, D8 Advance), SEM (FEI, Verios G4), AC-TEM (FEI, Themis Z), XPS (Kratos,

AXIS Ultra DLD), AFM (Bruker, Dimension Icon), Raman (WITec, Alpha 300R),

sXAS (Beamlines 7.3.1 and 8.0.1.4, Advanced Light Source, Berkeley). The

electrochemical properties of the developed Mn-OH, E-MO and E-MO/PPy were

evaluated on a CHI760E electrochemical workstation at room temperature, where a

three-electrode configuration was adopted with a Pt sheet electrode ($20\times20\times0.1$ mm^3)

as the counter electrode, an Ag/AgCl electrode as the reference electrode and 1 M

Na_2SO_4 aqueous solution as the electrolyte, respectively. The cycling measurement was

conducted on the Land CT2001A battery test system. The specific capacitance (C, F g^{-1}) was determined based on the galvanostatic charge/discharge curves by the following

equation:

$C=It/m\Delta V$ (3)

Here, I (A), m (g), t (s) and ΔV (V) represent the current, active mass, discharge time and the voltage window without the IR drop, respectively.

ASSOCIATED CONTENT

The Supporting Information is available free of charge at xxx.

Supplementary synthesis and calculation methods. Additional characterization information and notes of the microstructure evolution through EOEP or electrochemical oxidation process. Additional electrochemical analysis and the comparison between the performance of E-MO/PPy and the results in literature.

AUTHOR CONTRIBUTIONS

W.G. and Q.Z. proposed the research idea, designed the experimental procedures. W.G., C.D. and Q.Z. led the writing. W.G. guided material synthesis and characterizations. C.Z. performed the theoretical calculation and analysis. W.G., C.D., F.Y., J.U. and J.G. conducted the investigation, data curation, validation and contributed to the writing. All authors discussed the results and commented on the writing of the manuscript.

REFERENCES

1. Simon, P.; Gogotsi, Y., Perspectives for electrochemical capacitors and related devices. *Nat. Mater.* **2020**, *19*, 1151-1163.
2. Sun, H.; Zhu, J.; Baumann, D.; Peng, L.; Xu, Y.; Shakir, I.; Huang, Y.; Duan, X., Hierarchical 3D electrodes for electrochemical energy storage. *Nat. Rev. Mater.* **2018**, *4*, 45-60.
3. Dou, Q.; Wu, N.; Yuan, H.; Shin, K. H.; Tang, Y.; Mitlin, D.; Park, H. S., Emerging trends in anion storage materials for the capacitive and hybrid energy storage and beyond. *Chem. Soc. Rev.* **2021**, *50*, 6734-6789.
4. Zhong, M.; Zhang, M.; Li, X., Carbon nanomaterials and their composites for supercapacitors. *Carbon Energy* **2022**, *4*, 950-985.
5. Choi, C.; Ashby, D. S.; Butts, D. M.; DeBlock, R. H.; Wei, Q.; Lau, J.; Dunn, B., Achieving high energy density and high power density with pseudocapacitive materials. *Nat. Rev. Mater.* **2020**, *5*, 5-19.
6. Fleischmann, S.; Mitchell, J. B.; Wang, R.; Zhan, C.; Jiang, D.-e.; Presser, V.; Augustyn, V., Pseudocapacitance: from fundamental understanding to high power energy storage materials. *Chem. Rev.* **2020**, *120*, 6738-6782.
7. Fleischmann, S.; Zhang, Y.; Wang, X.; Cummings, P. T.; Wu, J.; Simon, P.; Gogotsi, Y.; Presser, V.; Augustyn, V., Continuous transition from double-layer to Faradaic charge storage in confined electrolytes. *Nat. Energy* **2022**, *7*, 222-228.
8. Liu, F.; He, J.; Liu, X.; Chen, Y.; Liu, Z.; Chen, D.; Liu, H.; Zhou, W., MoC nanoclusters anchored Ni@N-doped carbon nanotubes coated on carbon fiber as three-dimensional and multifunctional electrodes for flexible supercapacitor and self-heating device. *Carbon Energy* **2021**, *3*, 129-141.
9. Yang, W.; Zhang, C.; Du, S.; Jiang, B.; Wang, C.; Bai, H.; Li, Z.; Huang, G.; Li, Y., Potentiostatic reconstruction of nickel-cobalt hydroxysulfate with self-optimized structure for enhancing energy storage. *Adv. Energy Mater.* **2022**, *12*, 2202286.
10. Ning, M.; Zhang, F.; Wu, L.; Xing, X.; Wang, D.; Song, S.; Zhou, Q.; Yu, L.; Bao, J.; Chen, S.; Ren, Z., Boosting efficient alkaline fresh water and seawater electrolysis via electrochemical reconstruction. *Energy Environ. Sci.* **2022**, *15*, 3945-3957.
11. Li, Z. H.; Duan, H. H.; Shao, M. F.; Li, J. B.; O'Hare, D.; Wei, M.; Wang, Z. L., Ordered-vacancy-induced cation intercalation into layered double hydroxides: a general approach for high-performance supercapacitors. *Chem* **2018**, *4*, 2168-2179.
12. Guo, W.; Yang, F.; Yu, C.; Xie, Y.; Chen, J.; Liu, Y.; Zhao, Y.; Yang, J.; Feng, X.; Li, S.; Wang, Z.; Yu, J.; Liu, K.; Qian, K.; Tsige, M.; Zhang, Q.; Guo, J.; Qiu, J., *Operando* leaching of pre-incorporated Al and mechanism in transition-metal hybrids on carbon substrates for enhanced charge storage. *Matter* **2021**, *4*, 2902-2918.
13. Luo, H.; Wang, L.; Ren, P.; Jian, J.; Liu, X.; Niu, C.; Chao, D., Atomic engineering promoted electrooxidation kinetics of manganese-based cathode for stable aqueous zinc-ion batteries. *Nano Res.* **2022**, *15*, 8603-8612.

14.   Lei, J.; Yao, Y.; Wang, Z.; Lu, Y.-C., Towards high-areal-capacity aqueous zinc–manganese batteries: promoting MnO_2 dissolution by redox mediators. *Energy Environ. Sci.* **2021**, *14*, 4418-4426.

15.   Li, S.; Sharma, N.; Yu, C.; Zhang, Y.; Wan, G.; Fu, R.; Huang, H.; Sun, X.; Lee, S. J.; Lee, J. S.; Nordlund, D.; Pianetta, P.; Zhao, K.; Liu, Y.; Qiu, J., *Operando* tailoring of defects and strains in corrugated beta-Ni(OH)$_2$ nanosheets for stable and high-rate energy storage. *Adv. Mater.* **2021**, *33*, 2006147.

16.   Zhao, Q.; Song, A.; Ding, S.; Qin, R.; Cui, Y.; Li, S.; Pan, F., Preintercalation strategy in manganese oxides for electrochemical energy storage: review and prospects. *Adv. Mater.* **2020**, *32*, 2002450.

17.   Qin, L.; Tao, Q.; Liu, X.; Fahlman, M.; Halim, J.; Persson, P. O. Å.; Rosen, J.; Zhang, F., Polymer-MXene composite films formed by MXene-facilitated electrochemical polymerization for flexible solid-state microsupercapacitors. *Nano Energy* **2019**, *60*, 734-742.

18.   Zhang, M.-Y.; Song, Y.; Yang, D.; Qin, Z.; Guo, D.; Bian, L.-J.; Sang, X.-G.; Sun, X.; Liu, X.-X., Redox poly-counterion doped conducting polymers for pseudocapacitive energy storage. *Adv. Funct. Mater.* **2021**, *31*, 2006203.

19.   Jia, Y.; Chen, S.; Meng, X.; Peng, X.; Zhou, J.; Zhang, J.; Hong, S.; Zheng, L.; Wang, Z.; Bielawski, C. W.; Geng, J., Growing electrocatalytic conjugated microporous polymers on self-standing carbon nanotube films promotes the rate capability of Li–S batteries. *Small* **2023**, 2303919.

20.   Memon, M. A.; Bai, W.; Sun, J.; Imran, M.; Phulpoto, S. N.; Yan, S.; Huang, Y.; Geng, J., Conjunction of conducting polymer nanostructures with macroporous structured graphene thin films for high-performance flexible supercapacitors. *ACS Appl. Mater. Interfaces* **2016**, *8*, 11711-11719.

21.   Xiong, P.; Wu, Y.; Liu, Y.; Ma, R.; Sasaki, T.; Wang, X.; Zhu, J., Two-dimensional organic–inorganic superlattice-like heterostructures for energy storage applications. *Energy Environ. Sci.* **2020**, *13*, 4834-4853.

22.   Zhao, Y.; Zhou, R.; Song, Z.; Zhang, X.; Zhang, T.; Zhou, A.; Wu, F.; Chen, R.; Li, L., Interfacial designing of MnO_2 half-wrapped by aromatic polymers for high-performance aqueous zinc-ion batteries. *Angew. Chem. Int. Ed.* **2022**, *61*, e202212231.

23.   Lei, Q.; Zhang, J.; Liang, Z.; Yue, Y.; Ren, Z.; Sun, Y.; Yao, Z.; Li, J.; Zhao, Y.; Yin, Y.; Huai, P.; Lv, Z.; Li, J.; Jiang, Z.; Wen, W.; Li, X.; Zhou, X.; Zhu, D., Synergistic engineering of sulfur vacancies and heterointerfaces in copper sulfide anodes for aqueous Zn‑ion batteries with fast diffusion kinetics and an ultralong lifespan. *Adv. Energy Mater.* **2022**, *12*, 2200547.

24.   Zhang, Z.; Xi, B.; Wang, X.; Ma, X.; Chen, W.; Feng, J.; Xiong, S., Oxygen defects engineering of $VO_2 \cdot xH_2O$ nanosheets via in situ polypyrrole polymerization for efficient aqueous zinc ion storage. *Adv. Funct. Mater.* **2021**, *31*, 2103070.

25.   Zhao, J.; Xu, S.; Tschulik, K.; Compton, R. G.; Wei, M.; O'Hare, D.; Evans, D. G.; Duan, X., Molecular-scale hybridization of clay monolayers and conducting polymer for thin-film supercapacitors. *Adv. Funct. Mater.* **2015**, *25*, 2745-2753.

26.   Todd, E. C.; Sherman, D. M.; Purton, J. A., Surface oxidation of pyrite under ambient atmospheric and aqueous (pH = 2 to 10) conditions: electronic structure and mineralogy from X-ray absorption spectroscopy. *Geochim. Cosmochim. Acta* **2003**, *67*, 881-893.

27.   Azioune, A.; Siroti, F.; Tanguy, J.; Jouini, M.; Chehimi, M. M.; Miksa, B.; Slomkowski, S., Interactions and conformational changes of human serum albumin at the surface of electrochemically synthesized thin polypyrrole films. *Electrochim. Acta* **2005**, *50*, 1661-1667.

28.   Ramakrishnan, S.; Park, B.; Wu, J.; Yang, W.; McCloskey, B. D., Extended interfacial stability through simple acid rinsing in a Li-rich oxide cathode material. *J. Am. Chem. Soc.* **2020**, *142*, 8522-8531.

29.   Dai, K.; Wu, J.; Zhuo, Z.; Li, Q.; Sallis, S.; Mao, J.; Ai, G.; Sun, C.; Li, Z.; Gent, W. E.; Chueh, W. C.; Chuang, Y.-d.; Zeng, R.; Shen, Z.-x.; Pan, F.; Yan, S.; Piper, L. F. J.; Hussain, Z.; Liu, G.; Yang, W., High reversibility of lattice oxygen redox quantified by direct bulk probes of both anionic and cationic redox reactions. *Joule* **2019**, *3*, 518-541.

30.   Shan, X.; Guo, F.; Charles, D. S.; Lebens-Higgins, Z.; Abdel Razek, S.; Wu, J.; Xu, W.; Yang, W.; Page, K. L.; Neuefeind, J. C.; Feygenson, M.; Piper, L. F. J.; Teng, X., Structural water and disordered structure promote aqueous sodium-ion energy storage in sodium-birnessite. *Nat. Commun.* **2019**, *10*, 4975.

31.   Zhu, S.; Wang, Y.; Zhang, J.; Sheng, J.; Yang, F.; Wang, M.; Ni, J.; Jiang, H.; Li, Y., Jahn-Teller effect directed bandgap tuning of birnessite for pseudocapacitive application. *Energy Environ. Mater.* **2022**, DOI: 10.1002/eem2.12382.

32.   Yao, S.; Wang, S.; Liu, R.; Liu, X.; Fu, Z.; Wang, D.; Hao, H.; Yang, Z.; Yan, Y.-M., Delocalizing the d-electrons spin states of Mn site in MnO_2 for anion-intercalation energy storage. *Nano Energy* **2022**, *99*, 107391.

33.   Zhang, J.; Li, W.; Wang, J.; Pu, X.; Zhang, G.; Wang, S.; Wang, N.; Li, X., Engineering p-band center of oxygen boosting H^+ intercalation in δ-MnO_2 for aqueous zinc ion batteries. *Angew. Chem. Int. Ed.* **2022**, *62*, e202215654.

34.   Menezes, P. W.; Walter, C.; Hausmann, J. N.; Beltrán-Suito, R.; Schlesiger, C.; Praetz, S.; Yu. Verchenko, V.; Shevelkov, A. V.; Driess, M., Boosting water oxidation through in situ electroconversion of manganese gallide: an intermetallic precursor approach. *Angew. Chem. Int. Ed.* **2019**, *58*, 16569-16574.

35.   Guo, W.; Yu, C.; Li, S.; Song, X.; Huang, H.; Han, X.; Wang, Z.; Liu, Z.; Yu, J.; Tan, X.; Qiu, J., A universal converse voltage process for triggering transition metal hybrids in situ phase restruction toward ultrahigh-rate supercapacitors. *Adv. Mater.* **2019**, *31*, 1901241.

36.   Zhao, C.; Yu, C.; Qiu, B.; Zhou, S.; Zhang, M.; Huang, H.; Wang, B.; Zhao, J.; Sun, X.; Qiu, J., Ultrahigh rate and long-life sodium-ion batteries enabled by engineered surface and near-surface reactions. *Adv. Mater.* **2018**, *30*, 1702486.

37.   Li, K.; Wang, X.; Wang, X.; Liang, M.; Nicolosi, V.; Xu, Y.; Gogotsi, Y., All-pseudocapacitive asymmetric MXene-carbon-conducting polymer supercapacitors. *Nano Energy* **2020**, *75*, 104971.

38.   Yang, L.; Cheng, S.; Wang, J.; Ji, X.; Jiang, Y.; Yao, M.; Wu, P.; Wang, M.; Zhou, J.; Liu, M., Investigation into the origin of high stability of δ-MnO_2 pseudo-capacitive electrode using operando Raman spectroscopy. *Nano Energy* **2016**, *30*, 293-302.

39.   Yao, S.; Zhao, R.; Wang, S.; Zhou, Y.; Liu, R.; Hu, L.; Zhang, A.; Yang, R.; Liu, X.; Fu, Z.; Wang, D.; Yang, Z.; Yan, Y.-M., Ni-doping induced structure distortion of MnO_2 for highly efficient Na^+ storage. *Chem. Eng. J.* **2022**, *429*, 132521.

40.   Boyd, S.; Ganeshan, K.; Tsai, W.-Y.; Wu, T.; Saeed, S.; Jiang, D.-e.; Balke, N.; van Duin, A. C. T.; Augustyn, V., Effects of interlayer confinement and hydration on capacitive charge storage in birnessite. *Nat. Mater.* **2021**, *20*, 1689-1694.

41.   Julien, C.; Massot, M.; Baddour-Hadjean, R.; Franger, S.; Bach, S.; Pereira-Ramos, J. P., Raman spectra of birnessite manganese dioxides. *Solid State Ionics* **2003**, *159*, 345-356.

42.   Zhang, A.; Zhao, R.; Hu, L.; Yang, R.; Yao, S.; Wang, S.; Yang, Z.; Yan, Y.-M., Adjusting the coordination environment of Mn enhances supercapacitor performance of MnO_2. *Adv. Energy Mater.* **2021**, *11*, 2101412.

43.   Pu, S.; Wang, Z.; Xie, Y.; Fan, J.; Xu, Z.; Wang, Y.; He, H.; Zhang, X.; Yang, W.; Zhang, H., Origin and regulation of self-discharge in MXene supercapacitors. *Adv. Funct. Mater.* **2023**, *33*, 2208715.

44.   Shi, Y.; Gao, S.; Yuan, Y.; Liu, G.; Jin, R.; Wang, Q.; Xu, H.; Lu, J., Rooting MnO_2 into protonated g-C_3N_4 by intermolecular hydrogen bonding for endurable supercapacitance. *Nano Energy* **2020**, *77*, 105153.

45.   Jia, H.; Cai, Y.; Lin, J.; Liang, H.; Qi, J.; Cao, J.; Feng, J.; Fei, W., Heterostructural graphene quantum dot/MnO_2 nanosheets toward high-potential window electrodes for high-performance supercapacitors. *Adv. Sci.* **2018**, *5*, 1700887.

46.   Peng, H.; Huang, S.; Tranca, D.; Richard, F.; Baaziz, W.; Zhuang, X.; Samorì, P.; Ciesielski, A., Quantum capacitance through molecular infiltration of 7,7,8,8-tetracyanoquinodimethane in metal–organic framework/covalent organic framework hybrids. *ACS Nano* **2021**, *15*, 18580-18589.

47.   Zhan, C.; Pham, T. A.; Cerón, M. R.; Campbell, P. G.; Vedharathinam, V.; Otani, M.; Jiang, D.-e.; Biener, J.; Wood, B. C.; Biener, M., Origins and implications of interfacial capacitance enhancements in C_{60}-modified graphene supercapacitors. *ACS Appl. Mater. Interfaces* **2018**, *10*, 36860-36865.

48.   Zhan, C.; Neal, J.; Wu, J.; Jiang, D.-e., Quantum effects on the capacitance of graphene-based electrodes. *J. Phys. Chem. C* **2015**, *119*, 22297-22303.

49.   Campbell, P. G.; Merrill, M. D.; Wood, B. C.; Montalvo, E.; Worsley, M. A.; Baumann, T. F.; Biener, J., Battery/supercapacitor hybrid via non-covalent functionalization of graphene macro-assemblies. *J. Mater. Chem. A* **2014**, *2*, 17764-17770.

50.   Song, Y.; Pan, Q.; Lv, H.; Yang, D.; Qin, Z.; Zhang, M.-Y.; Sun, X.; Liu, X.-X., Ammonium-ion storage using electrodeposited manganese oxides. *Angew. Chem. Int. Ed.* **2021**, *60*, 5718-5722.

For Table of Contents Only